Dam Break Flow Benchmarks: Quo Vadis?

Giordano Lipari
Watermotion | Waterbeweging
Zwolle, The Netherlands
glnl@ymail.com

Andrea Colagrossi
Institute of Marine Engineering
CNR – National Research Council
Rome, Italy
andrea.colagrossi@cnr.it

***Abstract*—SPH has widened the scope of simulations of dam-break flows beyond the primary focus on impact loads. The flow complexity – involving boundary layers, air phase, surface tension, bubble and droplet formation, nonstationary, inhomogeneous and anisotropic turbulence – still imposes a piecemeal modelling approach to both two- and three-dimensional studies.**

Here, two-dimensional simulations provide fresh insights into the capability of SPH to reproduce vortical and acoustic features after increasing the sole spatial resolution.

A dam-break flow on a dry floor and impacting a vertical wall has been resolved up to $\mathrm{Re}_{\mathrm{eff}} = 256{,}000$. The array of spatial resolutions $d/\Delta x = 800, 1600, 3200, 6400$ shows the emergence by nonlinearity of progressively smaller flow scales. Fluid particles can populate the viscous sublayer and resolve boundary layer separations.

Also, in the stages of chaotic motion, the intricate soundscape of acoustic waves and pulses supported by the weakly compressible fluid is resolved cleanly. The frequency bands in the pattern-bearing spectra of pressure signals help diagnose both causal and spurious flow events occurred during a simulation. The efficacy of density diffusion and viscosity in abating disturbances below the scale of the kernel diameter is apparent.

Experiments are needed to address all flow stages and validate highly resolved 2D and 3D simulations of dam breaks. The available measurements do not cover the agitated stages, while only pressure loads regard the impingement stages. The configuration of new apparatuses could be optimized for a high return of relevant detail from the compute elements (SPH particles), so that simulations can produce densely informative datasets.

I. A Benchmark for Sudden Water Arrivals

The sudden arrival of water masses flowing over a surface can be a violent phenomenon in many situations in civil, coastal, nautical and offshore engineering. Examples occur on the decks of ships, platforms and breakwaters as waves top over the freeboard; in channels as sluice gates release excess water from a reservoir or when a retaining structure fails; and along the shore as bores, tsunamis and swashes advance.

Dam-break flows denote a category of experimental and numerical benchmarks to study such flow situations by removing the partition that keeps a boxful of water at rest. The imbalance of forces on the water mass initiates the motion at the sides of the partition location, with a surface depression travelling upstream and a water wedge surging downstream (Fig. 1). At the level of global energy considerations, dam-break flows are isolated systems in a fixed reference frame. Monitoring the system evolution using the balance of mechanical energy is thus simpler than in systems where external work maintains the motion, like wave-and-current flumes and sloshing tanks.

At the level of detailed phenomenology, a dam-break flow in a closed tank consists of several interlocked stages [15]. After release, the surging flow is a stream and bore. After the impact with the tank or any objects placed in it, the free surface breaks up, generates cavities, and oscillates in cycles of splashing and sloshing. Therefore, besides the design configuration, the walls, air phase, and surface tension each influence pressure loads and flow velocities. The wall boundary layers and the plunging and spilling of the surface water generate and inject vorticity into the fluid bulk. The latter forcing is non-stationary, inhomogeneous and anisotropic, and is not amenable to the conventional frameworks for turbulence.

The principal modelling challenges are the flow three-dimensionality, the inclusion of the air phase and the interface physics. Addressing them in once is hampered by the saturation of the compute resources. Including air, to improve the free-surface motion and pressure loads, and capturing smaller eddy structures, to improve the interior dynamics, appear to be mutually exclusive objectives. Currently, the Reynolds numbers typical of fully developed turbulent regimes can be approached in single-phase 2D simulations only; modelling two-phase systems imposes that the mixing dynamics remains coarsely resolved in 2D and 3D. Variable-resolution methods can carve out room for progress between these two extremes.

These remarks lead the interpretation of the simulation results in § III-A (flow fields) and § III-B (point signals).

II. Simulation Workflow

We restrict ourselves to a single-phase dam-break flow on a dry floor and impacting a vertical wall ('dam break' for short). The 2D reduction of the apparatus of [4] and [13], shown in Fig. 1, is studied in dimensionless form after normalisation by d, g, μ, ρ, where d is the water column height at rest. The scales for speed, time and pressure are $\sqrt{gd}$, $\sqrt{d/g}$ and $\rho g d$.

Enforcing the weakly compressible behaviour with $\mathrm{Ma} = 0.1$ implies $c_0 = 10\sqrt{gd}$. Upon expressing the physical viscosity in terms of the artificial viscosity parameter α for two-dimensional flows [19], the SPH formulation of the Reynolds number is $8\frac{\mathrm{Ma}}{\alpha}\frac{d}{h}$. This formula yields the effective Reynolds number, $\mathrm{Re}_{\mathrm{eff}}$, that a simulation can solve directly. For set α and $h/\Delta x$, the spatial resolution $d/\Delta x$ thus scales with the turbulence-resolving power of the particle cloud.

The GPU acceleration strategy of DualSPHysics [8] enabled us to scale up the spatial resolution in the steps $d/\Delta x = 800$, 1600, 3200, 6400; see Tab. I for the compute size. The flow

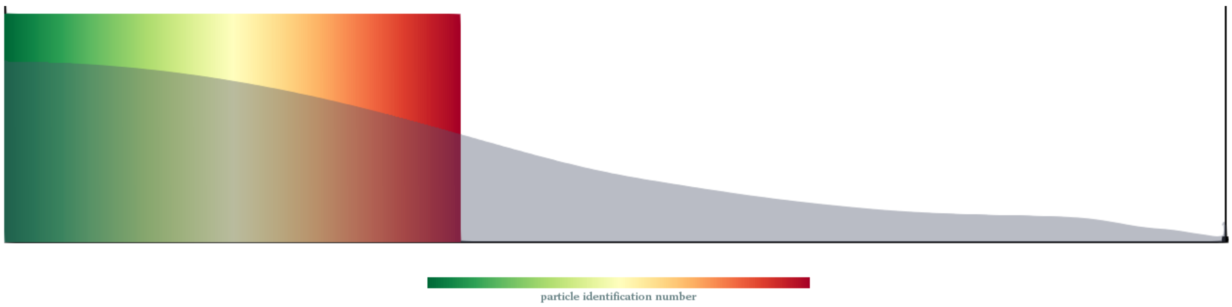

Fig. 1. Domain configuration. View size: $5.366\,d \times 1\,d$. Size of fluid reservoir at rest: $2\,d \times 1\,d$. The colour shades encode an immutable particle tag. The greener, the further back in the position at the outset; yellow shades are in the middle; the redder, the further to the front. Gray overlay: fluid mass at $2.4\,\sqrt{d/g}$, just after the impingement on the wall. The black marker on the lower downstream wall indicates a numerical pressure probe (see analysis in § III-B).

TABLE I
SPATIAL RESOLUTION, COMPUTE SIZE, AND PARAMETERS OF 2D TURBULENT FLOW. $h/\Delta x = 2$; $\alpha = 0.01$; SIMULATED TIME: $20\,\sqrt{d/g}$

$d/\Delta x$	800	1600	3200	6400
h/d (10^{-3})	2.50	1.25	0.625	0.3125
Fluid particles (10^3)	1,280	5,120	20,480	81,920
Time levels (10^3)	1,396	2,863	5,729	11,743
Average time step (10^{-6})	13.60	6.845	3.432	1.678
$\mathrm{Re}_{\mathrm{eff}}$	32,000	64,000	128,000	256,000
y_τ/d (10^{-3})	1.104	0.656	0.390	0.232
$y_\tau/\Delta x$	0.88	1.05	1.25	1.49
$5\,y_\tau/1.5h$	1.47	1.75	2.08	2.48

solver DualSPHysics is free software distributed under a LGPL licence [10]. [1] The physical and numerical settings were chosen to allow as close a comparison as possible with [17, § 5.2]. The equation of state is linear. The shifting correction has been disabled. The δ-type density-diffusion term implements an artificial diffusivity formulation [18] rather than a renormalized density gradient [23], which we expect not to hamper the energy transfer across flow scales. The 'dynamic boundary conditions' implement a repulsive force that keeps the fluid particles away from the wall at a case-dependent distance, in the order of $1.5h$ [9]; unlike the pure free-slip condition implemented in [17], the near-boundary fluid particles undergo viscous friction. In the artificial-viscosity formulation of the viscous term, the functional π_{ij} according to [20] – devised to alleviate anomalies in astrophysical shock problems – has been replaced with the expression in [17]:

$$\pi_{ij} = \frac{(\mathbf{u}_i - \mathbf{u}_j) \cdot (\mathbf{r}_i - \mathbf{r}_j)}{(\mathbf{r}_i - \mathbf{r}_j)^2}.$$

Importantly, this functional is consistent with the Laplacian and operates on pairs of approaching and separating particles alike: the dissipative physics in the inner fluid is thus scaled appropriately as flow structures become smaller, which supports the insights of § III-A. Here, $\alpha = 0.01$, while the sensitivity to its values is discussed in [17]. The resulting $\mathrm{Re}_{\mathrm{eff}}$ at each spatial resolution are shown in Tab. I.

The chosen time-marching method is a Verlet scheme instead of a modified Runge-Kutta with frozen diffusive approach. The time step for stability is tuned to acoustic and viscous lengthscales; the Courant coefficient C is 0.125. The simulated time is $20\,\sqrt{d/g}$, like [17]. The flow fields have been saved every $0.1\,\sqrt{d/g}$. Fixed numerical probes in the walls and in the fluid recorded the pressure and velocity signals every time step.

The redistribution of the DualSPHysics version 5.0.164 (27-11-2020) used for these simulations, the source code patches, the input settings, the runtime log files, and the output flow fields at each resolution are publicly available under a CC BY 4.0 licence [12]. These flow fields underlie the analysis of § III-A.[2] The signals underlying § III-B and results up to $30\,\sqrt{d/g}$ have not been published yet. More analyses than the selection presented here are under way.

This post-processing software has been used for this study: for visualisation: Matplotlib 3.5.0, ParaView 5.4.1; for signal analysis: Numpy 1.21.2; for producing the ParaView input data of velocity, density, particle tags and vorticity: PartVTK 5.0.122, a closed-source tool in the DualSPHysics suite.

III. Selected Simulation Results

A. Flow Fields

1) Boundary layer separations: The flow opposition at the location of detachment of a boundary layer can generate a stagnation point and promote circulating patterns in the inner flow, by action of viscosity. Two instances of an evolving boundary layer separation are visible in Fig. 2, on the floor next to the corner and on the vertical wall at mid height. On the floor, the stream raising up the wall after the impact (Fig. 1) has let an adverse gradient of (hydrostatic) pressure build up near the corner, which opposes the flow advancing

[1] In fulfilment of the licensing terms, this study implies neither endorsement nor promotion of DualSPHysics. The citation of DualSPHysics implies neither endorsement nor promotion of this study from the DualSPHysics contributors.

[2] Supplementary animations of the velocity, density and mixing fields simulated at each resolution are available at https://www.youtube.com/playlist?list=PLb_klyJ6w5QihDlztSqN0GRhT7awNnibe.

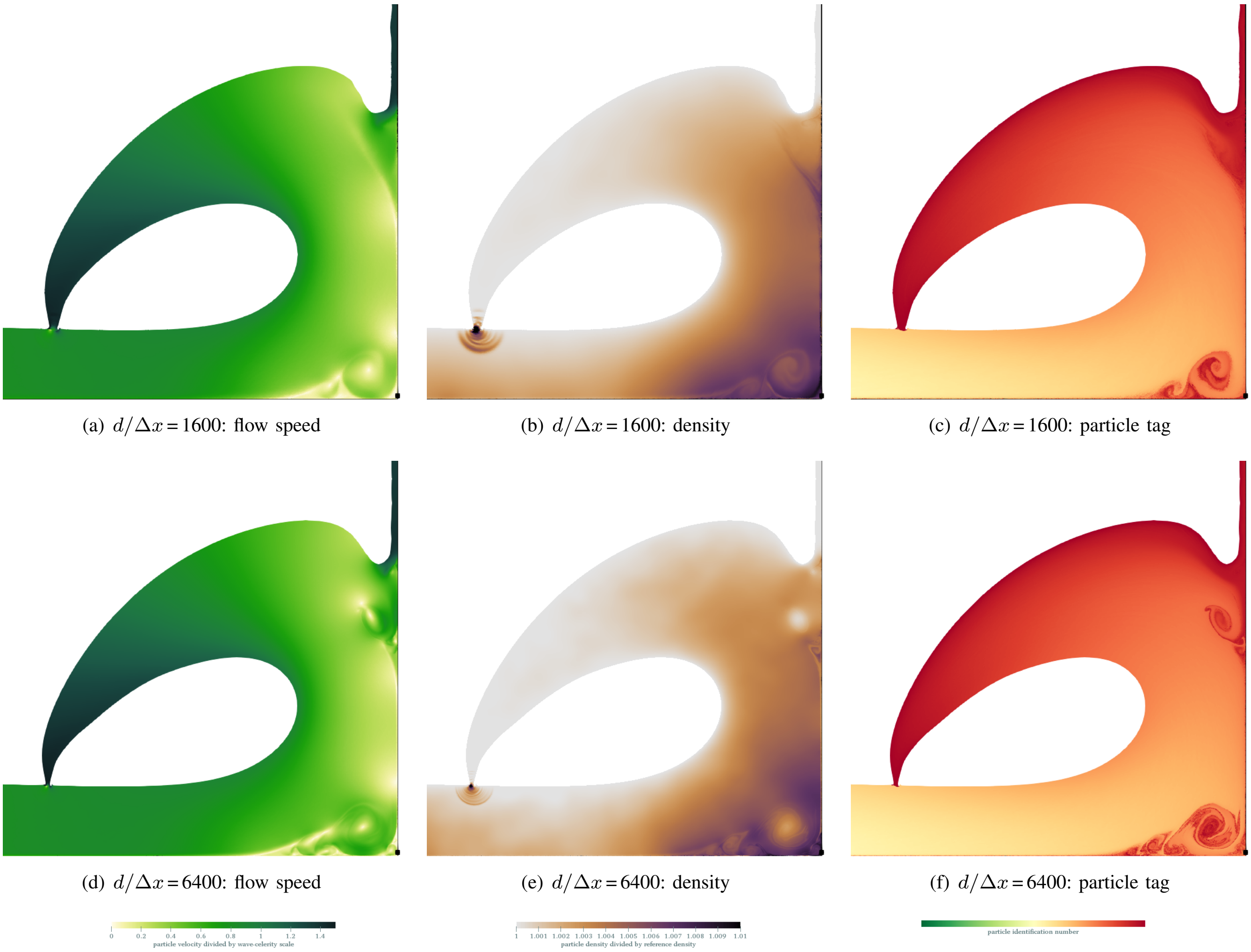

(a) $d/\Delta x = 1600$: flow speed (b) $d/\Delta x = 1600$: density (c) $d/\Delta x = 1600$: particle tag

(d) $d/\Delta x = 6400$: flow speed (e) $d/\Delta x = 6400$: density (f) $d/\Delta x = 6400$: particle tag

Fig. 2. The closure of the plunging jet and instances of boundary layer separation in the corner and off the wall. Time $6.1\sqrt{d/g}$; view size $1.266\,d \times 1.266\,d$. Individual particles are rendered with the same point size to represent the number density evenly. Compare with $d/\Delta x = 800$ in [17, Fig. 28].

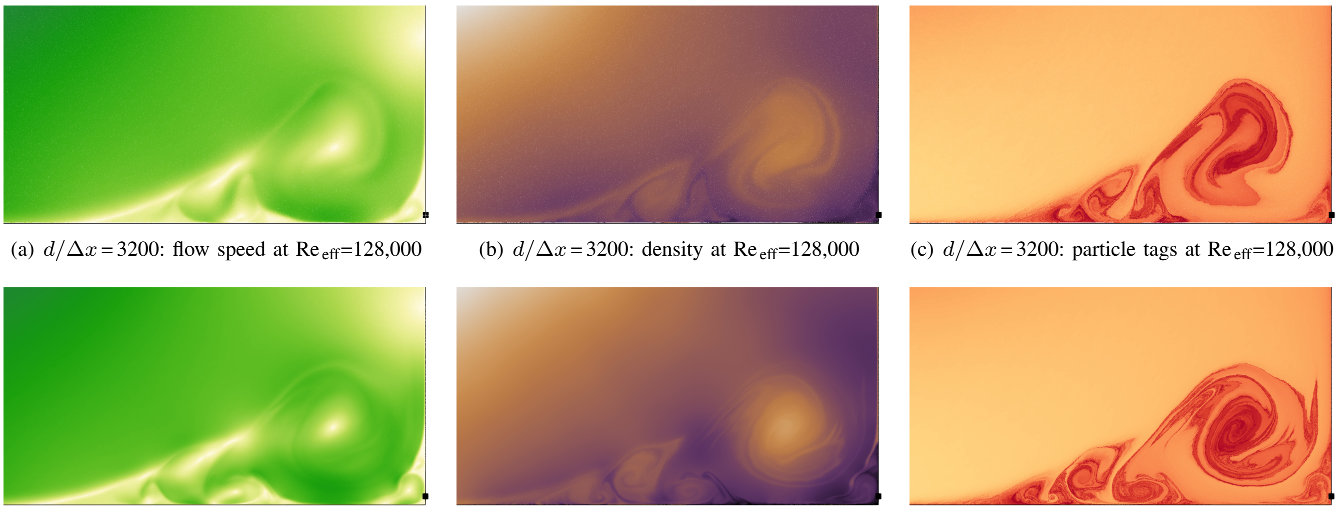

(a) $d/\Delta x = 3200$: flow speed at $\mathrm{Re}_{\mathrm{eff}}$=128,000 (b) $d/\Delta x = 3200$: density at $\mathrm{Re}_{\mathrm{eff}}$=128,000 (c) $d/\Delta x = 3200$: particle tags at $\mathrm{Re}_{\mathrm{eff}}$=128,000

(d) $d/\Delta x = 6400$: flow speed at $\mathrm{Re}_{\mathrm{eff}}$=256,000 (e) $d/\Delta x = 6400$: density at $\mathrm{Re}_{\mathrm{eff}}$=256,000 (f) $d/\Delta x = 6400$: particle tags at $\mathrm{Re}_{\mathrm{eff}}$=256,000

Fig. 3. Flow pattern at the floor-and-wall corner. Time $6.1\sqrt{d/g}$; view size: $0.55\,d \times 0.26\,d$ ($1409\,y_\tau \times 666\,y_\tau$ at $\mathrm{Re}_{\mathrm{eff}} = 128{,}000$; $2370\,y_\tau \times 1120\,y_\tau$ at $\mathrm{Re}_{\mathrm{eff}} = 256{,}000$). Same colour scales and rendering as Fig. 2.

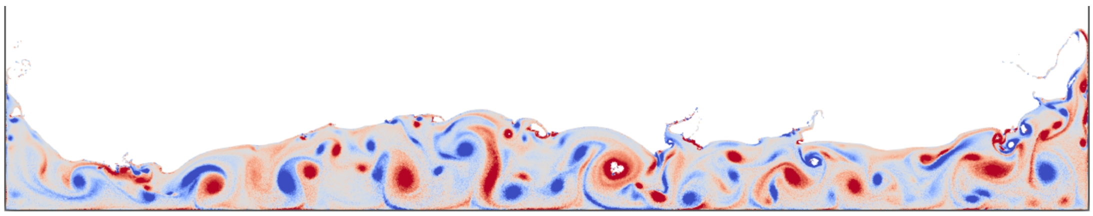

(a) $d/\Delta x = 800$, $\mathrm{Re}_{\mathrm{eff}}$=32,000

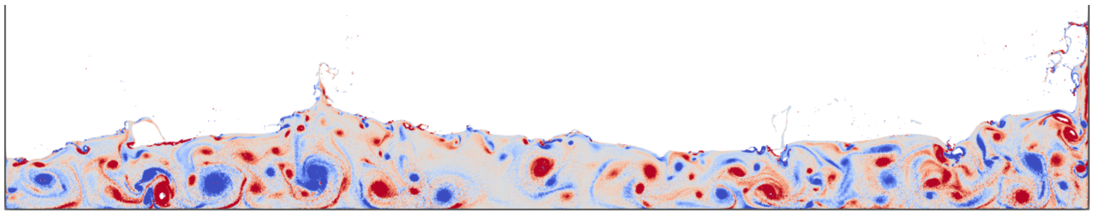

(b) $d/\Delta x = 1600$, $\mathrm{Re}_{\mathrm{eff}}$=64,000

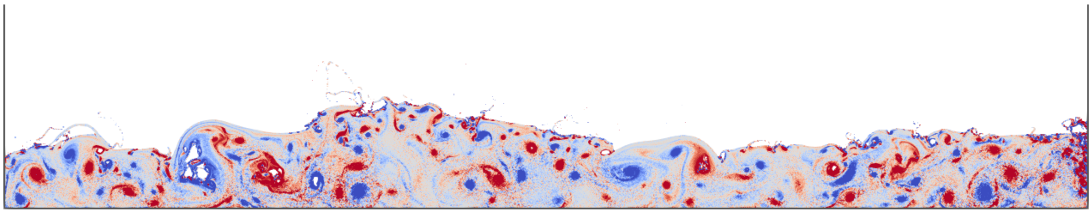

(c) $d/\Delta x = 3200$, $\mathrm{Re}_{\mathrm{eff}}$=128,000

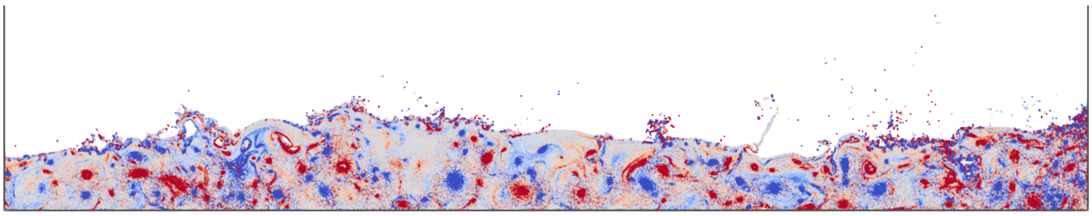

(d) $d/\Delta x = 6400$, $\mathrm{Re}_{\mathrm{eff}}$=256,000

Fig. 4. Vorticity field (scaled $\sqrt{g/d}$) in the sloshing stage. Time: 20 $\sqrt{d/g}$; view size: $5.366\,d \times 1\,d$. Compare with $d/\Delta x = 100$-1600 in [17, Fig. 24].

from the collapsing volume. On the vertical wall, the fluid has turned downwards after having reached its maximum height and forms a stream with a flow velocity of about $1.5\sqrt{gd}$ that wedges into the flank of the plunging jet. Both separations can be recognized from multiple flow patterns. First, low-speed regions identify the stagnation points at the wall, streaks of decelerated water, and the centres of the recirculating regions in Figs. 2(a), 2(d). Second, in Figs. 2(b), 2(e), the density minima identify the centres of recirculating regions, and the density maxima the impingements. Third, the colour shades in Figs. 2(c), 2(f) show that the plunging jet and the recirculating regions contain water particles arrived early on, together with the surge leading edge. [3] Interestingly, the setting $d/\Delta x = 1600$ still resolves poorly the separation off the vertical wall.

2) Approaching the viscous sublayer: The enhanced spatial resolution allows the fluid particles to populate the viscous wall region down to the viscous sublayer, as shown in Tab. I. [4] Recalling § II, the wall boundary conditions then approximate a no-slip condition. Additionally, the consistent Laplacian operator ensures that the action of the viscous terms is gauged with the spatial resolution. Fig. 3 zooms into the corner area at the same instant as Fig. 2 and at the two highest resolutions, $d/\Delta x = 3200, 6400$; the view size in wall units is reported

[3] The colour shades do not indicate a metric for the mixing intensity. They mark the provenance of the particle from within the reservoir at rest, as shown in Fig. 1. The red particles are those arrived with the first impact.

[4] We estimated the viscous lengthscale $y_\tau = \nu/u_\tau$ with the Blausius law for zero-pressure-gradient boundary layers developing on a smooth plate $u_\tau^2 = 0.332\,U^2\,\mathrm{Re}_x^{-0.5}$, which gives $y_\tau = 1.736\,d\,(L/d)^{0.25}\,\mathrm{Re}_{\mathrm{eff}}^{-0.75}$ for a plate of length L. The approximation is considerable insofar as the boundary layer in a dam-break flow is unsteady.

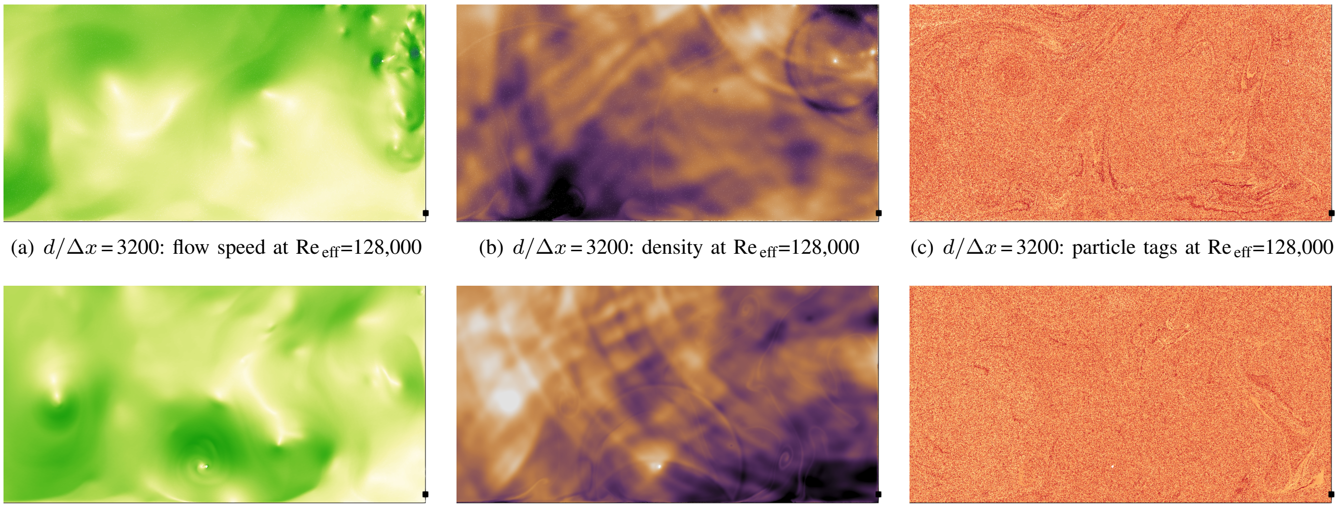

(a) $d/\Delta x = 3200$: flow speed at $\mathrm{Re}_{\mathrm{eff}}$=128,000
(b) $d/\Delta x = 3200$: density at $\mathrm{Re}_{\mathrm{eff}}$=128,000
(c) $d/\Delta x = 3200$: particle tags at $\mathrm{Re}_{\mathrm{eff}}$=128,000
(d) $d/\Delta x = 6400$: flow speed at $\mathrm{Re}_{\mathrm{eff}}$=256,000
(e) $d/\Delta x = 6400$: density at $\mathrm{Re}_{\mathrm{eff}}$=256,000
(f) $d/\Delta x = 6400$: particle tags at $\mathrm{Re}_{\mathrm{eff}}$=256,000

Fig. 5. Flow pattern at the floor-and-wall corner. Time: $20\sqrt{d/g}$. Same view, colour scales and rendering as Fig. 3.

in the caption. Doubling $\mathrm{Re}_{\mathrm{eff}}$ from 128,000 to 256,000 reproduces finer details upstream of the vortical structures that deflect the incoming fluid away from the corner; in the ambient fluid entrained into the separated region; and in the corner's recess, where a tiny vortex forms. Significant variations of pressure and shear stress on the floor and wall can be inferred.

3) Chaotic motion: The approximations of neglecting air and surface tension cease to be realistic after the first void cavity seals off at $6.1\sqrt{d/g}$, as displayed in Fig. 2. As already established for the resolution $d/\Delta x = 400$ [15], the air cushions the water impacts and maintains bubbles inside the fluid bulk, thus steering the system towards a different path than the single-phase system. Regardless, the transfer of the initial potential energy towards smaller vortical structures intensifies, in a chaotic manner, as the spatial resolution increases; the distributions of vorticity at $20\sqrt{d/g}$ in Fig. 4 are progressively finer, although not homogeneous over the domain. In this stage the free surface breaks weakly, intermittently and locally, while the sloshing between the two ends of the tank settles slowly.

Owing to the chaotic agitation, in the long run similar flow structures are unlikely to be stably located in the same places for all spatial resolutions. Nonetheless, the simulations should express at a finer scale the capabilities and limitations expected from the modelling. With this expectation in mind, Fig. 5 shows the same quantities and views as Fig. 3 at the time of Fig. 4, $20\sqrt{d/g}$. In detail, the density of Figs. 5(b), 5(e) presents the pattern of acoustic disturbances travelling across the domain with the speed of sound c_0 and reflected by the walls. These are generated inside the field of view – for example, by the spurious cavitation of a void pocket that produces a radiating compressional pulse – as well as outside of it – for example, as wave fronts triggered by impacts at the free surface, like in Figs. 2(b), 2(e). The superposition of streak-like patterns mirroring the local flow and of ring-like acoustic waves is particularly clear in Fig. 5(e). Such a soundscape matches the behaviour expected from a weakly compressible fluid. Then, Figs. 5(c), 5(f) show that, at the highest spatial resolution, mixing has further broken up the clusters of fluid particles with nearby provenance. The supplementary animations indicate that patches of unmixed fluid can persist elsewhere.

4) Notes on direct turbulence modelling: The resolution at $d/\Delta x = 6400$ brings to 256,000 the maximum effective Reynolds number in a dam-break flow simulation; this is also close to $\mathrm{Re} = 516{,}000$ in the measurements of [13]. The previous documented maximum was $\mathrm{Re}_{\mathrm{eff}} = 64{,}000$ [17].

These new highly resolved simulations narrow the gap between the anticipated and resolved flow scales. The internal dynamics, the mixing processes and their cumulative effects are resolved more detailedly. Interestingly, while the smallest scales in the inner fluid remain unresolved, fluid particles can populate the viscous sublayer, at least according to a back-of-the-envelope scaling. This capability is attractive for applications sensitive to the distribution and evolution of shear stresses and pressures near a boundary: for example, mobilisable beds, as well as unwanted structural loads and noise. Also, this analysis provides an intuition to evaluate, say in the simulation planning for a particular project, whether a gain in resolution justifies its compute overheads.

A note of caution regards the two-dimensional turbulence. Smaller vortical features constrained to live on a plane can coalesce into larger features in an inverse energy cascade not supported by the three-dimensional space [3]. Finally, it should not be taken for granted either that a single Reynolds number applies to each stage of the dam-break flow, since the pressure gradients driving the initial surge and the following stages differ, and their flow scales may differ accordingly.

B. Pressure Measurements at the Wall

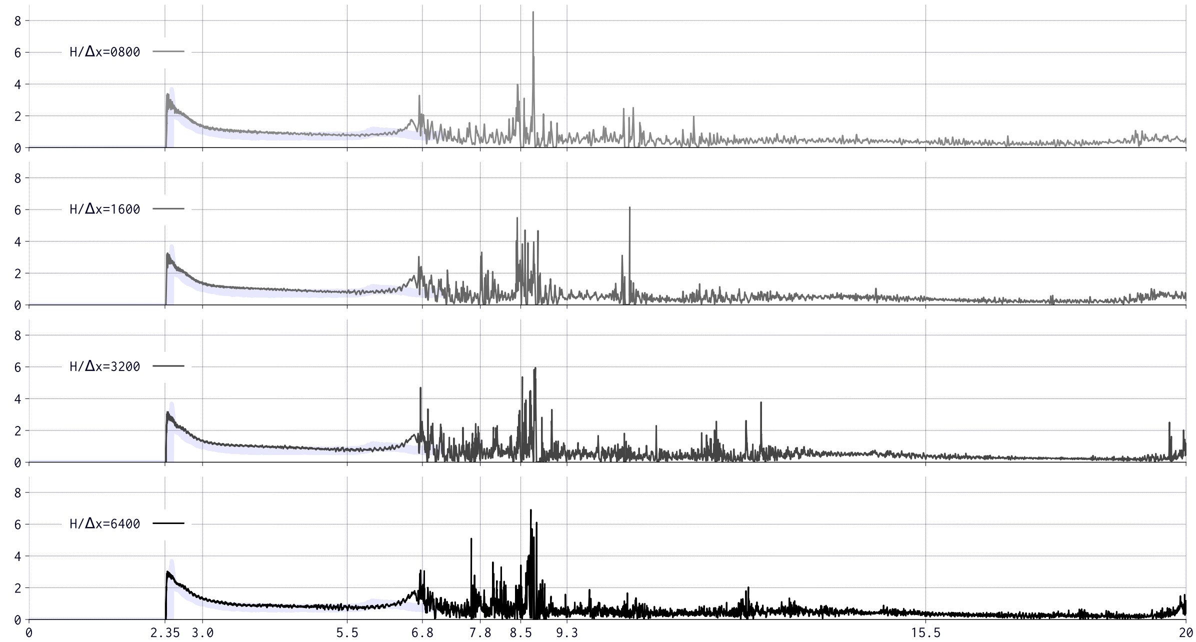

Fig. 6. Raw time signals of the average pressure at a numerical probe on the wall: time (scaled $\sqrt{d/g}$) versus pressure (scaled $\rho g d$); axes in linear scale. The time-axis ticks mark the moment of impingement and when the kinetic and potential energies attain relative maxima/minima according to [17, Fig. 9].

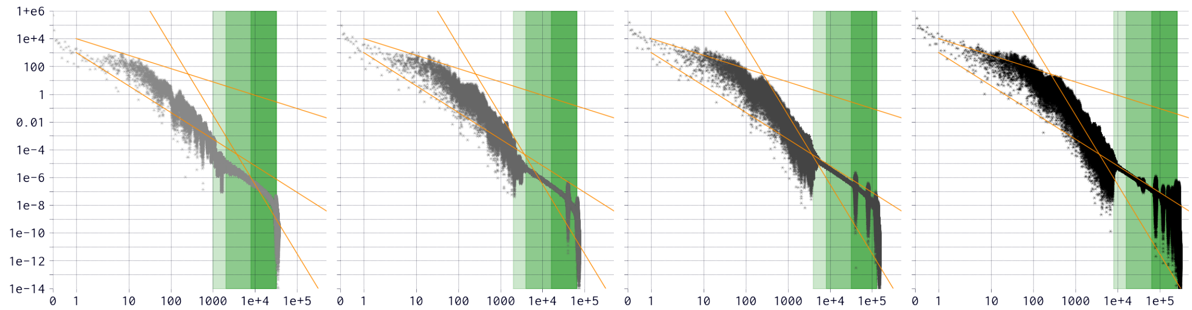

Fig. 7. Discrete power spectra of the average pressure at a numerical probe on the wall; frequency (scaled $\sqrt{g/d}$) versus spectral power (scaled $(\rho g d)^2$); abscissas in symmetric log scale, ordinates in log scale. Panels, rightwards: $d/\Delta x = 800, 1600, 3200, 6400$. Slopes: -1, -2, -5. Shaded areas, rightwards: frequencies bands $f > c_0/4h$, $f > c_0/2h$, $f > c_0/\Delta x$ and $f < c_0/(C\,h)$, where C is the Courant coefficient.

1) Signals in the time domain: We comment on the signal of the average pressure on a probe in the wall at $z = 0.01\,d$, as done in the experimental apparatus [13]. [5] This location is shown in the previous figures. The pressure is proportional to the density fields of Fig. 2 and Fig. 5 after the linear equation of state. Fig. 6 shows the time histories of pressure at each spatial resolution. The shaded area indicates the variability in the measurements, which only cover the first 7 $\sqrt{d/g}$ seconds [13]. The simulated impacts occur before the measured one: the events could be matched by tuning the friction acting on the near-wall particles via the viscosity parameter α (§ II). The effect of friction on the initial surge indeed is a long-standing topic in dam-break research [5]–[7], [11], [21]. Also, the peak signals feature excursions early on that confuse the evaluations of convergence and the agreement with the measurements.

2) Spectra in the frequency domain: We then inspect the discrete power spectra transforming the full-length pressure signals with a FFT, shown in Fig. 7. [6]

[5] A spatially averaged pressure has been computed dividing the force normal to a sensing line of length $4h$ centred in the nominal location by the line size. The variable probe size captures approximately the same number of particles at each spatial resolution and forestalls an undersampling bias.

[6] A usage note about the term 'power' is in order here. The power referred to in signal analysis does not bear in itself such mechanical meaning as the temporal rate of change of an energy content. The (spectral) power is the squared amplitude of a single-frequency component, considered as complex number. The discrete power of a spectrum is the summation of the powers of its discrete components. A spectrum's power is thus a measure of the space between the spectrum and the supporting abscissas; for a pressure signal in

TABLE II
PRESSURE RECORDS AT A NUMERICAL PROBE AT $z = 0.01\,d$ IN THE WALL. SPECTRAL POWER METRICS AND CHARACTERISTIC FREQUENCIES.

f: frequency; S: total spectrum power; S_a: low-pass power at cut-off $f = a\,\mathrm{Hz}$; $s_a = \frac{S_a - S_0}{S - S_0}$; f_a: cut-off frequency giving the low-passed power aS. Signal duration: $20\sqrt{d/g}$. Physical units in dimensional form for clarity.

$d/\Delta x$	-	800	1600	3200	6400
$\mathrm{Re}_{\mathrm{eff}}$	-	32,000	64,000	128,000	256,000
no. components	10^3	629	1,297	2,604	5,359
$f_{\max}$	kHz	36	74	148	304
S	$10^5\,\mathrm{Pa}^2$	6.486	13.73	27.12	54.15
S_0	$10^5\,\mathrm{Pa}^2$	4.955	10.52	20.17	41.60
S_0/S	-	.763	.765	.744	.768
s_{50}	-	.981	.960	.938	.919
s_{100}	-	.996	.986	.980	.968
s_{250}	-	.999	.996	.992	.987
$f_{0.995}$	Hz	94	232	296	420
$c_0/4h$	kHz	1	2	4	8
$c_0/2h$	kHz	2	4	8	16
$c_0/\Delta x$	kHz	8	16	32	64
$c_0/(C\,h)$	kHz	32	64	128	256

The temporal evolution of the spectral content could be elicited with techniques such as wavelet transforms, as proposed to filter SPH results [16]. The time step scales with h/c_0, which doubles the Nyquist maximum frequency as the spatial resolution doubles. [7] Tab. II shows that the number of components, the resolved frequency bands, and the total spectrum power, S, double. The power of the zero-frequency component, S_0, is the sum of the discrete signals of Fig. 6 and takes up nearly three quarters of the total spectrum power at all spatial resolutions. Further, the role of the oscillating components is quantified with two metrics, shown in Tab. II. First, the quantity s determines how far the power components below chosen cut-off frequencies fill the gap between S_0 and S at each spatial resolution: as the latter increases, the cut-off frequencies 50, 100, 250 Hz do low-pass smaller portions of the spectrum gap consistently. Second, the cut-off frequency low-passing a spectrum the power of which is 99.5% of the total, $f_{0.995}$, grows with the spatial resolution. Therefore, higher spatial resolutions enrich the pressure signal with a wider range of densely spaced components, that is more and finer active timescales. Interestingly, the upper bounds of the bands describing most of the power spectra are between 94 and 420 Hz, out of resolved bands hundreds of kHz wide.

The spectra of Fig. 7 clearly show that, for all spatial resolutions, the power decays in a six-band pattern with variable values and slopes. At very low frequencies (0-1 Hz) the power components drop by two to three orders of magnitude. At low frequencies the slopes are between –1 and –2; at intermediate frequencies around –5, alongside diffused power excursions as wide as three orders of magnitude; and at high frequencies closely –2, alongside a modest power variability. (Trends with same slope may overlap.) At very high frequencies the spectrum spikes up within a few narrow bands and, finally, dies off.

The frequencies naturally associated via c_0 with the SPH lengthscales — the kernel diameter $4h$, the smoothing length h and the particle spacing Δx — support the pattern interpretation. The green-shaded areas in Fig. 7 indicate the high-frequency bands above $c_0/4h$ (light shade), $c_0/2h$ (medium shade), and $c_0/\Delta x$ (deeper shade) up to a frequency related to the numerical stability limit, $c_0/(C\,h)$. Only when $d/\Delta x = 3200, 6400$ are oscillations shorter than the kernel diameter free of large power excursions. In contrast, when $d/\Delta x = 800, 1600$, those excursions spill over a transition band from the intermediate frequencies into the in-kernel frequencies; this could be interpreted as noise due to coarsely resolved physics. Further, besides from probe averaging, the smooth decay and the –2 slope in the high-frequency bands above $c_0/4h$ could result from the density-diffusion term, which characteristically dampens progressive acoustic waves at the kernel scale [1]. In the very-high-frequency band above $c_0/\Delta x$, the pattern of 'tones' is the more pervasive, the higher the spatial resolution. (Weaker tones stand out in the kernel-size band when $d/\Delta x = 6400$.) The underlying events might relate to the impulses of particle-sized spray showering the fluid and to the spurious pulses of condensation/rarefaction following the formation/implosion of void pockets, captured in Figs. 5(b), 5(e). Finally, only the viscous contribution can create frequencies beyond $c_0/(C\,h)$ by further constraining the time step for stability; consistently, the component powers vanish into numerical nil in those tailing bands.

3) Note on pressure spectra as a diagnostic tool for simulations: The spectra of pressure signals provide a finely-resolved, patterned footprint of the soundscape of waves and pulses traversing the SPH fluid at the speed of sound c_0, even when the motion is chaotic. The dependencies on the spatial resolution become apparent. Conveniently, SPH-related frequency scales help conjecture the originating mechanism of the acoustic disturbances (waves versus pulses, causal versus spurious) as well as identify the efficacy of density diffusion and viscosity in abating high-frequency motion. Therefore, the transformed pressure signals promise to be an inexpensive and uncomplicated diagnostic tool to examine the net outcome of very expensive SPH simulations, as it were, by auscultation.

IV. FORWARD-LOOKING REMARKS

We have shown that highly resolved SPH can approach the direct numerical simulations of two-dimensional hydrodynamics, providing detailed insights into the separation of unsteady boundary layers and the soundscape of a weakly compressible fluid.

dimensional units, this power is measured in Pa^2. We do not discuss the power spectral density either, that is the 'power' contained in a single oscillation at each frequency, with units $\mathrm{Pa}^2/\mathrm{Hz}$.

[7] The signal recorded at a variable time step is first interpolated on an equispaced sequence of as many time levels as the simulations (Tab. I). Detrending is unnecessary since the pressure signals are not cyclical.

Dam-break flows are a multi-phase, multi-scale, multi-stage benchmark relevant for many engineering applications. Introduced 130 years ago in the form of a *Dammbruchkurve* by the astrophysicist August Ritter as an application of shallow-water dynamics in infinite channels [24], they have grown into a benchmark for impulsive actions. Numerical investigations have then widened their scope beyond the impingement into stages where the free-surface breaking and internal friction determine the flow. There, extended three-dimensional and two-phase simulations resolving wide ranges of eddy motions are still hampered by the problematic triad of air phase, interface processes, and dimensionality.

Here, the configuration for surges on a dry floor impacting a vertical wall has been simulated without the air phase for $\mathrm{Re}_{\mathrm{eff}} = 256{,}000$ and with $d/\Delta x = 6400$ upon tracking 82 million particles, using 13 GB memory of a single compute-capable GPU, and taking an average 54 runtime hours to simulate each physical second. High spatial resolution also involves other upscaling challenges, such as the storage, transfer and analysis of larger and denser datasets describing the flow closely enough [12]. And high-performance computing with hardware acceleration will arguably afford us simulations with ever more SPH particles. As for experiments, alas, no measurements regard the agitated stages, and only pressure data cover the impingement stages.

Perhaps, this imbalance in the state of the art could act as a stimulus to design new apparatuses that are computationally reproducible, in which most of the capital of computable particles yields maximum insight into relevant flow dynamics at minimum compute loads. To that end, we imagine that the computationally ideal experiment of a dam-break flow strikes an optimum between several desiderata: 1) having a minimal reservoir volume; 2) compressing the sloshing and settling stage in as short a time as possible; 3) having small three-dimensional effects and, even better, positively approximating a two-dimensional flow, in view of the behaviour of turbulence; 4) recording water elevation, pressure and velocities during the entire process, with point and field measurements; 5) consisting of several repetitions to work around the unsteady and chaotic behaviour; 6) enclosing the air phase.

Acknowledgements

The simulations have been performed thanks to Prof. C. Vuik at the Delft Institute of Applied Mathematics in the Delft University of Technology. The collection of datasets [12] are publicly available courtesy of the 4TU.ResearchData repository in the Netherlands. The latest version of this article and its figures are available at https://doi.org/10.5281/zenodo.6391457 under a CC BY 4.0 licence.

References

[1] M. Antuono, A. Colagrossi, S. Marrone, and D. Molteni, Free-surface flows solved by means of SPH schemes with numerical diffusive terms, Computer Physics Communications, vol. 181, no. 3, pp. 532-549, Mar. 2010.

[2] M. Antuono, S. Marrone, and A. Colagrossi, Violent wave impacts and loadings using the δ-SPH method, in Advanced Numerical Modelling of Wave Structure Interactions, 1st ed., D. M. Kelly, A. Dimakopoulos, and P. Higuera, Eds. First edition. 1 Boca Raton, FL: CRC Press/Taylor & Francis: CRC Press, 2021, pp. 121-147.

[3] G. Boffetta and R. E. Ecke, Two-dimensional turbulence, Annual Review of Fluid Mechanics, vol. 44, pp. 427-451, 2012.

[4] B. Buchner, Green water on ship-type offshore structures, Delft University of Technology, Delft, The Netherlands, 2002.

[5] O. Castro-Orgaz and H. Chanson, Ritter's dry-bed dam-break flows: positive and negative wave dynamics, Environ Fluid Mech, vol. 17, no. 4, pp. 665-694, Aug. 2017.

[6] H. Chanson, Tsunami surges on dry coastal plains: application of dam break wave equations, Coastal Engineering Journal, vol. 48, no. 4, pp. 355-370, Dec. 2006.

[7] H. Chanson, Application of the method of characteristics to the dam break wave problem, Journal of Hydraulic Research, vol. 47, no. 1, pp. 41-49, Jan. 2009.

[8] J. M. Domínguez, A. J. C. Crespo, and M. Gómez-Gesteira, Optimization strategies for CPU and GPU implementations of a smoothed particle hydrodynamics method, Computer Physics Communications, vol. 184, no. 3, pp. 617-627, Mar. 2013.

[9] J.M. Domínguez, G. Fourtakas, J.L. Cercos-Pita, R. Vacondio, B.D. Rogers, A.J.C. Crespo, Evaluation of reliability and efficiency of different boundary conditions in a SPH code, Proceedings of the 10th International SPHERIC Workshop, Parma, pp. 341-348, 2015.

[10] J.M. Domínguez, G. Fourtakas, C. Altomare, R.B. Canelas, A. Tafuni, O. García-Feal, I. Martínez-Estévez, A. Mokos, R. Vacondio, A.J.C. Crespo, R.D. Rogers, P.K. Stansby, M. Gómez-Gesteira, DualSPHysics: from fluid dynamics to multiphysics problems, Computational Particle Mechanics, 2021.

[11] R. F. Dressler, Hydraulic resistance effect upon the dam-break functions, Journal of Research of the National Bureau of Standards, vol. 49, no. 3, p. 217-225, Sep. 1952.

[12] G. Lipari and C. Vuik, High-resolution SPH simulations of a 2D dam-break flow against a vertical wall. 4TU.ResearchData, 23 Apr 2021. doi: https://doi.org/10.4121/c.5353691.

[13] L. Lobovský, E. Botia-Vera, F. Castellana, J. Mas-Soler, and A. Souto-Iglesias, Experimental investigation of dynamic pressure loads during dam break, Journal of Fluids and Structures, vol. 48, pp. 407-434, Jul. 2014.

[14] S. Marrone, M. Antuono, A. Colagrossi, G. Colicchio, D. Le Touzé, and G. Graziani, δ-SPH model for simulating violent impact flows, Computer Methods in Applied Mechanics and Engineering, vol. 200, no. 13-16, pp. 1526-1542, Mar. 2011.

[15] S. Marrone, A. Colagrossi, A. Di Mascio, and D. Le Touzé, Analysis of free-surface flows through energy considerations: Single-phase versus two-phase modeling, Phys. Rev. E, vol. 93, no. 5, p. 053113, May 2016.

[16] D. D. Meringolo, A. Colagrossi, S. Marrone, and F. Aristodemo, On the filtering of acoustic components in weakly-compressible SPH simulations, Journal of Fluids and Structures, vol. 70, pp. 1-23, Apr. 2017.

[17] D. D. Meringolo, S. Marrone, A. Colagrossi, and Y. Liu, A dynamic δ-SPH model: How to get rid of diffusive parameter tuning, Computers & Fluids, vol. 179, pp. 334-355, Jan. 2019.

[18] D. Molteni and A. Colagrossi, A simple procedure to improve the pressure evaluation in hydrodynamic context using the SPH, Computer Physics Communications, vol. 180, no. 6, pp. 861-872, Jun. 2009.

[19] J. J. Monaghan, Smoothed particle hydrodynamics, Rep. Prog. Phys., vol. 68, no. 8, pp. 1703-1759, Aug. 2005.

[20] J. J. Monaghan and R. A. Gingold, Shock simulation by the particle method SPH, Journal of Computational Physics, vol. 52, no. 2, pp. 374-389, Nov. 1983.

[21] I.-R. Park, K.-S. Kim, J. Kim, and S.-H. Van, Numerical investigation of the effects of turbulence intensity on dam-break flows, Ocean Engineering, vol. 42, pp. 176-187, Mar. 2012.

[22] S. B. Pope, Turbulent Flows. Cambridge, UK: Cambridge University Press, 2000.

[23] P. W. Randles and L. D. Libersky, Smoothed Particle Hydrodynamics: Some recent improvements and applications, Computer Methods in Applied Mechanics and Engineering, vol. 139, pp. 375-408, 1996.

[24] A. Ritter, Die Fortpflanzung der Wasserwellen, Zeitschrift des Vereines Deutscher Ingenieure, vol. 36, no. 2.33, pp. 947-954, 1892.